Assignment II Parabolic Reflector Antenna

EE4725 Quasi Optical Systems

Petar V. Peshev, p.v.peshev@student.tudelft.nl
Department of Electrical Engineering, Mathematics, and Computer Science,
Delft University of Technology, Delft, The Netherlands

Abstract

In this assignment, a parabolic reflector, with focal length $F = 3\ m$, is illuminated by a circular feed with diameter $D_{feed} = 4\lambda$. The antenna is considered to be in free space. Moreover, the circular feed has y-polarized and uniform equivalent electric current with unitary amplitude. Finally, the frequency of operation is $f = 50\ GHz$. The performance of this antenna geometry is analyzed over different diameters D of the parabolic reflector.

I. Feed Far-Field Pattern

For the circular feed's uniform y-polarized equivalent electric current $\vec{J}_{feed} = J_0\hat{y}$ (the current's amplitude is unitary, $J_0 = 1\ Am^{-2}$, however, it is generalized for any amplitude J_0 in the derivations), it can be shown that its Fourier Transform (FT) has an airy pattern

$$\tilde{\mathbf{J}}_{\mathbf{feed}}(k_x, k_y) = \iint_S \vec{J}_{feed}(\vec{r'})e^{jk\hat{r}\cdot\vec{r'}}dS = 2\pi a^2 J_0 \frac{\tilde{J}_1(ka\sin\theta)}{ka\sin\theta}\hat{y}, \tag{1}$$

where $\tilde{J}_1(x)$ is the Bessel's function of first order, k the propagation constant, and a the feed's radius. The feed is in free space (k is the free space propagation constant at $f = 50\ GHz$), and has a radius $a = 2\lambda$ (where λ is the wavelength). Moreover, an airy pattern has a main lobe at the center (airy disk) with concentric ring side lobes; consequently, the $\tilde{\mathbf{J}}_{\mathbf{feed}}$ magnitude is expected to be equal in the XZ and YZ-planes. Finally, for an airy pattern, the beamwidth is related to the wavelength and diameter

$$\theta_{BW} = \frac{\lambda}{D}, \tag{2}$$

where D is the circular's aperture diameter (generalized and valid for the reflector's and feed's aperture). Therefore, for $D_{feed} = 4\lambda$, the pattern is expected to contain four beams together with the main lobe.

The simulated $\tilde{\mathbf{J}}_{\mathbf{feed}}$ magnitude (in dB at $f = 50\ GHz$ and $D_{feed} = 4\lambda$) at $\phi = 0°, 180°$ (XZ-plane) and $\phi = 90°, 270°$ (YZ-plane) is plotted in Fig.1; the plot is normalized to the maximum value. The simulation coincide with the analytical expectations, the $\tilde{\mathbf{J}}_{\mathbf{feed}}$ magnitude is equal at $\phi = 0°, 180°$ and $\phi = 90°, 270°$, and the pattern consists of four beams.

In previous assignments, it is proved that the electric far-field $\vec{E}^{FF}$ is given by the multiplication of the Spectral Green's Function (SGF) and the source's current density FT

$$\vec{E}^{FF}(r, \theta, \phi) = jk_z\mathbf{G}^{\mathbf{EJ}}(k_x, k_y)\tilde{\mathbf{J}}(k_x, k_y)\frac{e^{-jkr}}{2\pi r}, \tag{3}$$

where k_x, k_y, and k_z are the x, y, and z-components of the dominant wave vector respectively, $\mathbf{G}^{\mathbf{EJ}}(k_x, k_y)$ is the dyadic SGF relating electric current density to $\vec{E}^{FF}$, and r is the radial distance between source and observation point. Moreover, it is also proved that $\mathbf{G}^{\mathbf{EJ}}$ is a function of the dominant wave vector and wave impedance

$$\mathbf{G}^{\mathbf{EJ}}(k_x, k_y) = -\frac{\eta}{2kk_z}\begin{bmatrix} k^2 - k_x^2 & -k_xk_y & -k_xk_z \\ -k_yk_x & k^2 - k_y^2 & -k_yk_z \\ -k_zk_x & -k_zk_y & k^2 - k_z^2 \end{bmatrix}, \tag{4}$$

where η is the wave impedance in the medium. From the circular feed's electric current density FT in Eq.1 and its relation to $\vec{E}^{FF}$ in Eq.3, the feed's electric far-field is calculated. Furthermore, as a consequence of the feed's current y-polarization, only the SGF_{xy}^{EJ}, SGF_{yy}^{EJ}, and SGF_{zy}^{EJ}-components partake in the calculation of $\vec{E}^{FF}$

$$E_x^{FF} \propto k_xk_y = k^2\sin^2\theta\frac{\sin 2\phi}{2}, \tag{5a}$$

$$E_y^{FF} \propto k^2 - k_y^2 = k^2(1 - \sin^2\theta\sin^2\phi), \tag{5b}$$

$$E_z^{FF} \propto k_zk_y = k^2\frac{\sin 2\theta}{2}\sin\phi. \tag{5c}$$

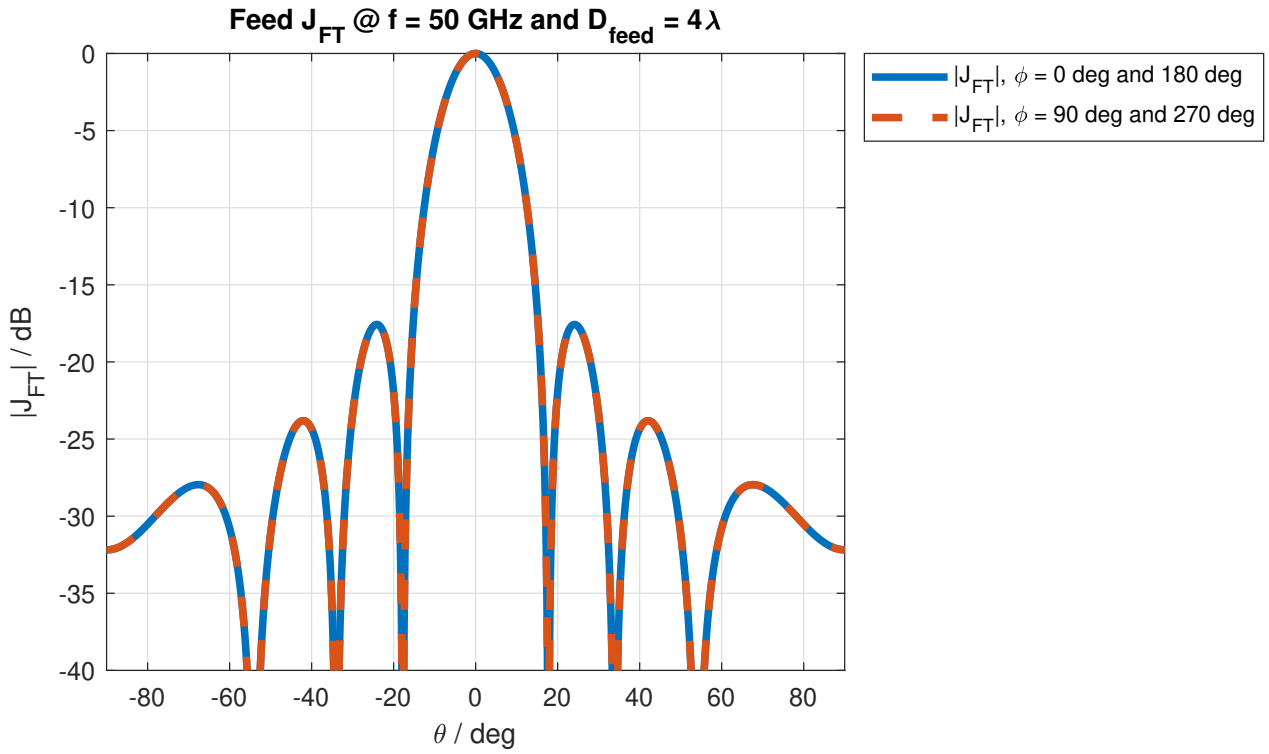

Fig. 1. Simulated feed's electric current density Fourier Transform $\tilde{\mathbf{J}}_{\mathbf{feed}}$ in decibels dB and normalized to the maximum value, for a frequency $f = 50\ GHz$ and feed diameter $D_{feed} = 4\lambda$, and plotted at $\phi = 0°, 180°$ (XZ-plane) and $\phi = 90°, 270°$ (YZ-plane)

As $\theta \to 90°$, the SGF_{xy}^{EJ} and SGF_{yy}^{EJ}-components become dominant

$$\lim_{\theta \to 90°} k_x k_y = k^2 \frac{\sin 2\phi}{2}, \tag{6a}$$

$$\lim_{\theta \to 90°} k^2 - k_y^2 = k^2(1 - \sin^2 \phi), \tag{6b}$$

$$\lim_{\theta \to 90°} k_z k_y = 0; \tag{6c}$$

under these considerations, Eq.6a has local minimums at $\phi = 0°, 90°, 180°, 270°$ and local maximums at $\phi = 45°, 135°, 225°, 315°$, while Eq.6b has local minimums at $\phi = 90°, 270°$ and local maximums at $\phi = 0°, 180°$. Further, the maximum of Eq.6b is two times larger than the maximum of Eq.6a. As a result of Eq.6a and 6b having local minimums at $\phi = 90°, 270°$, the magnitude of $\vec{E}^{FF}$ is expected to decrease as $\theta \to 90°$ and $\phi \to 90°$ or $\phi \to 270°$. Therefore, the feed's far-field does not have a properly defined airy pattern, due to each concentric side lobe varying as a function of ϕ. Moreover, the concentric side lobes are expected to have local minimums at $\phi = 90°, 270°$ (the last side lobe has zero magnitude at $\theta = 90°$ for these azimuth angles ϕ).

The simulated $\vec{E}_{feed}^{FF}$ pattern (in dB at $f = 50\ GHz$ and $D_{feed} = 4\lambda$) is plotted in Fig.2; the plot is normalized to the maximum value. The simulation coincide with the analytical expectations, the $\vec{E}_{feed}^{FF}$ is not a proper airy pattern, and the concentric side lobes have local maximums at $\phi = 0°, 180°$ and minimums at $\phi = 90°, 180°$. Furthermore, the simulated $\vec{E}_{feed}^{FF}$ magnitude (in dB at $f = 50\ GHz$ and $D_{feed} = 4\lambda$) at $\phi = 0°, 180°$ (XZ-plane) and $\phi = 90°, 270°$ (YZ-plane) is plotted in Fig.3; the plot is normalized to the maximum value. The *irregularity* in the airy pattern is clearly visualized. As expected from the analytical derivations, the mismatch between the XZ and YZ-plane is greatest for the last concentric side lobe, where $\theta = 90°$.

II. Equivalent Aperture Current Distribution

For the reflector's aperture field $\vec{E}_a$, it can be shown that its cylindrical coordinate's radial distance ρ and azimuth angle ϕ-components are equal to the negative spherical coordinate's elevation angle θ and azimuth angle ϕ-components of $\vec{E}_{feed}^{FF}$ respectively

$$\vec{E}_a = (-E_{feed}^{\theta}\hat{\rho} - E_{feed}^{\phi}\hat{\phi}) \frac{\cos^2 \frac{\theta'}{2}}{F} e^{-jk2F}, \tag{7}$$

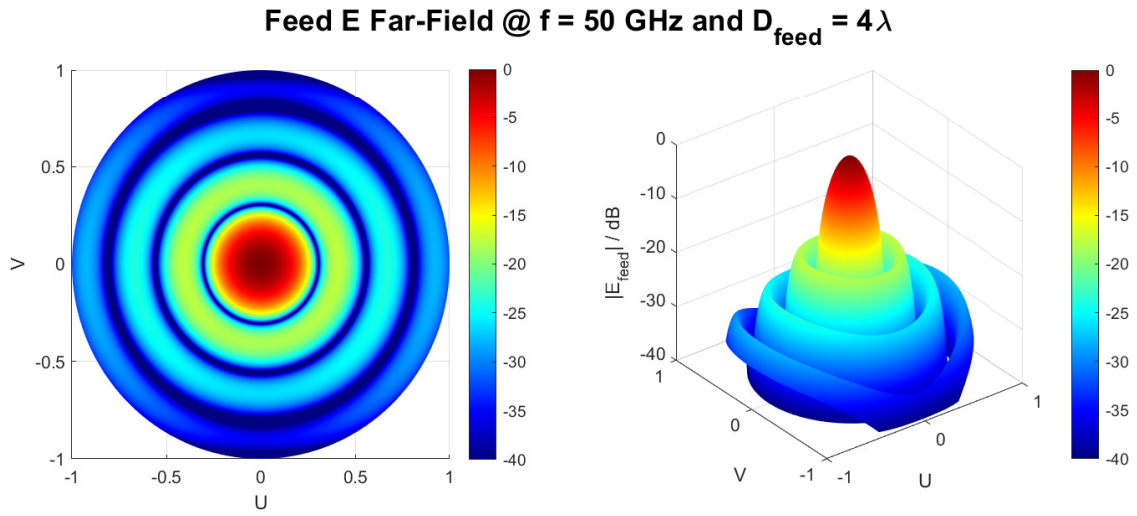

Fig. 2. Simulated feed's electric far-field $\vec{E}^{FF}_{feed}$ pattern in decibels dB and normalized to the maximum value, for a frequency $f = 50\ GHz$ and feed diameter $D_{feed} = 4\lambda$

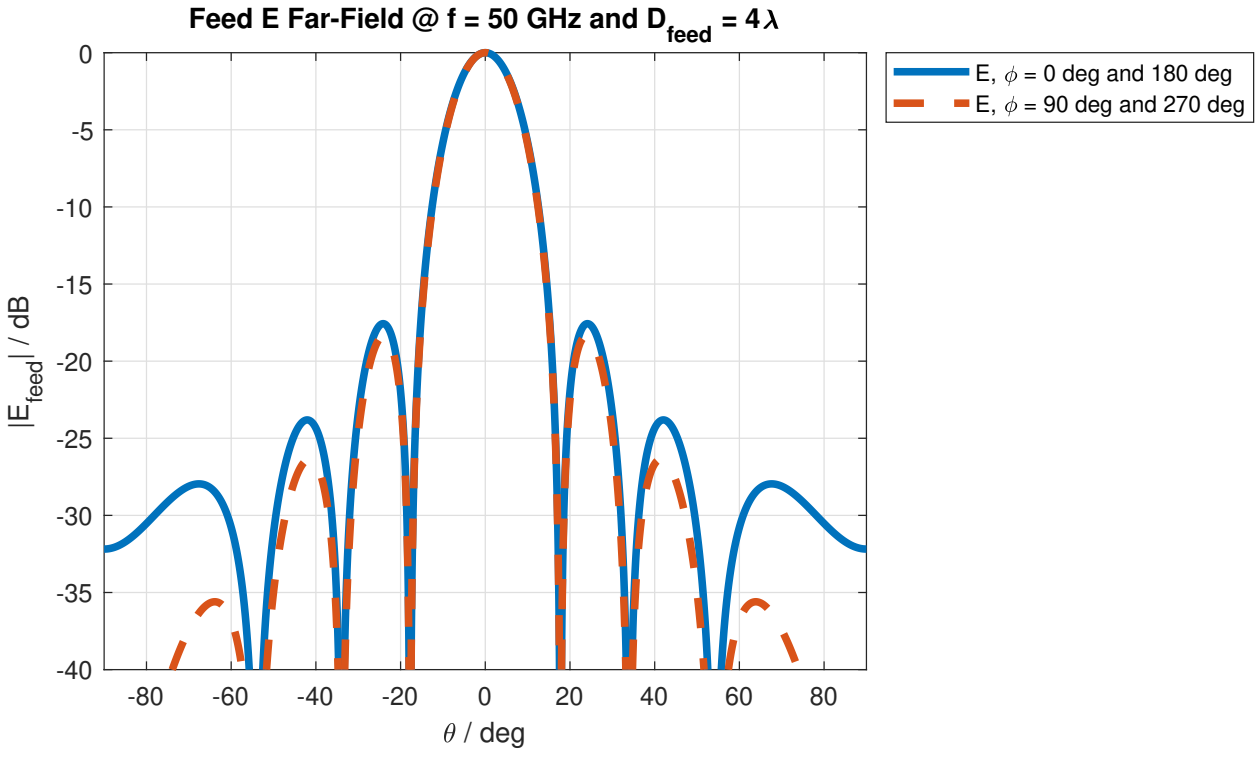

Fig. 3. Simulated feed's electric far-field $\vec{E}^{FF}_{feed}$ in decibels dB and normalized to the maximum value, for a frequency $f = 50\ GHz$ and feed diameter $D_{feed} = 4\lambda$, and plotted at $\phi = 0°, 180°$ (XZ-plane) and $\phi = 90°, 270°$ (YZ-plane)

where θ' is the angle between the reflector's normal and wave's propagation direction. Effectively, a transformation from spherical to cylindrical coordinates occurs when $\vec{E}^{FF}_{feed}$ is reflected at the reflector's interface. Additionally, the reflection at the perfect electric conductor (PEC) reverses the polarization, causing the negative signs in the $\vec{E}_a$ components. Furthermore, the phase of $\vec{E}_a$ is proportional to two times the focal length, and its amplitude is a function of θ' and the focal length. Finally, the aperture field's phase is constant over the horizontal plane.

The equivalent aperture current is calculated by applying the equivalence theorem at an interface between two free space mediums known as Love's formulation, or the equivalence and image theorems at an interface between free medium and perfect magnetic conductor (PMC) known as Schelkunoff's formulation. Consequently when using Love's formulation, the equivalent aperture magnetic current density is the cross product of the aperture's electric field and normal vector

$$\vec{M}_a \approx \vec{E}_a \times \hat{n}_a \mid_S; \tag{8}$$

while the electric current density is the cross product of the aperture's normal vector and magnetic field

$$\vec{J}_a \approx \hat{n}_a \times \vec{H}_a \mid_S = \frac{1}{\eta}\hat{r} \times (\hat{n}_a \times \vec{E}_a) \mid_S, \tag{9}$$

where the electric and magnetic fields are related through the Poynting's vector, and $\hat{r}$ is the direction of propagation of the aperture's wave. On the other hand, when using Schelkunoff's formulation, the magnetic current density is zero as a consequence of the image theorem at the boundary (the image has an opposite polarity to the actual magnetic current)

$$\vec{M}_a = 0\, V m^{-2}, \tag{10}$$

while the electric current density is twice the current density in Love's formulation (the image has the same polarity as the actual electric current)

$$\vec{J}_a \approx 2\hat{n}_a \times \vec{H}_a \mid_S = 2\frac{1}{\eta}\hat{r} \times (\hat{n}_a \times \vec{E}_a) \mid_S . \tag{11}$$

For the considered geometry, the aperture wave Poynting's vector and aperture's normal are both in the positive z-direction ($\hat{n}_a = \hat{z}$ and $\hat{r} = \hat{z}$). Therefore in Love's formulation, the x and y-components of $\vec{M}_a$ are proportional to the θ and ϕ-components of $\vec{E}^{FF}_{feed}$

$$M_x \propto -E^{\theta}_{feed} \sin\phi - E^{\phi}_{feed} \cos\phi, \tag{12a}$$

$$M_y \propto E^{\theta}_{feed} \cos\phi - E^{\phi}_{feed} \sin\phi. \tag{12b}$$

Due to E^{θ}_{feed} and E^{ϕ}_{feed} being in-phase for the x-component of $\vec{M}_a$ and out-of-phase for the y-component, the dominant component of $\vec{M}_a$ is in x. Therefore, the x-component is expected to have a much larger magnitude than the y-component, or the aperture's magnetic current density is mostly x-polarized. Moreover, by using the property $\vec{A}\times(\vec{B}\times\vec{C}) = (\vec{A}\cdot\vec{C})\vec{B} - (\vec{A}\cdot\vec{B})\vec{C}$, the magnitudes of the components of the electric current density are found to be the reverse of the magnetic current density components, $|J_x| = |M_y|$ and $|J_y| = |M_x|$. As a result, the electric current density is mostly y-polarized. Finally, in case the aperture has a comparable diameter to the main lobe of $\vec{E}_a$, $\vec{M}_a$ is uniform, as a consequence of reflecting only the main lobe of $\vec{E}^{FF}_{feed}$; on the other hand, as the diameter increases, the reflected side lobe power of $\vec{E}^{FF}_{feed}$ increases, consequently the non-uniformity of $\vec{E}_a$ increases, which results in a non-uniform $\vec{M}_a$. Therefore for larger diameters, $|\vec{M}_a|$ is expected to decrease with the radial distance.

The simulated x and y-components of $\vec{M}_a$ (in dB at $f = 50\, GHz$ and $D_{feed} = 4\lambda$) are plotted in Fig.4; the plot is normalized to the maximum values. The simulation coincides with the analytical expectations, the x-component of $\vec{M}_a$ decreases as the radial distance increases; a consequence, of the non-uniform aperture field caused by the large aperture diameter D. Further, each concentric side lobe is the result of the reflected respective $\vec{E}^{FF}_{feed}$ side lobe. Moreover, although the y-component of $\vec{M}_a$ has a zero decibel magnitude (result of the normalization to the component's maximum magnitude), the maximum value of the y-component is 43 decibels below the maximum value of the x-component (more than 140 times smaller in linear scale). Therefore, $\vec{M}_a$ is mostly x-polarized and $\vec{J}_a$ is mostly y-polarized.

III. Far-Field Pattern

From Eq.3, $\vec{E}^{FF}$ is calculated by using the FT of $\vec{J}_a$

$$\tilde{\mathbf{J}}_{\mathbf{a}}(k_x, k_y) = \iint_S \vec{J}_a(\rho', \phi') e^{jk_x\rho'\cos\phi'} e^{jk_y\rho'\sin\phi'} \rho' d\rho' d\phi', \tag{13}$$

where $\vec{J}_a(\rho', \phi')$ is a function of the radial distance ρ' and azimuth angle ϕ' as a result of the spherical to cylindrical coordinate transformation in Eq.7. The $\tilde{\mathbf{J}}_{\mathbf{a}}$ is not analytically derived, but numerically calculated in simulations. From Eq.2, θ_{BW} is expected to be small due to the large aperture diameter ($\theta_{BW} \approx 0.23^{\circ}$). However, $\vec{M}_a$ is not uniform (the reflector's

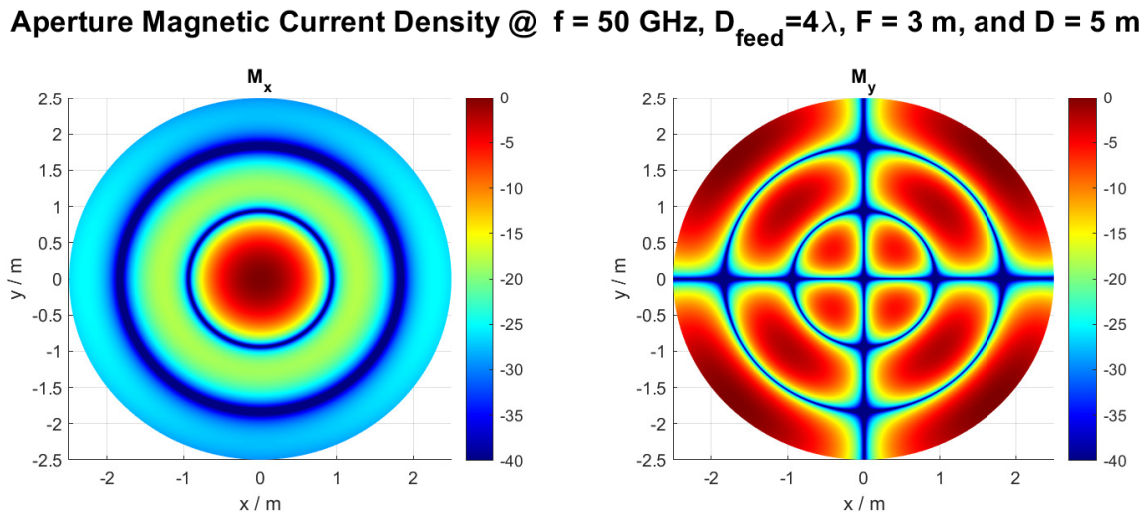

Fig. 4. Simulated x and y-components of the equivalent aperture magnetic current $\vec{M}_a$ in decibels dB and normalized to the maximum value, for a frequency $f = 50\ GHz$, feed diameter $D_{feed} = 4\lambda$, aperture diameter $D = 5\ m$, and focal length $F = 3\ m$

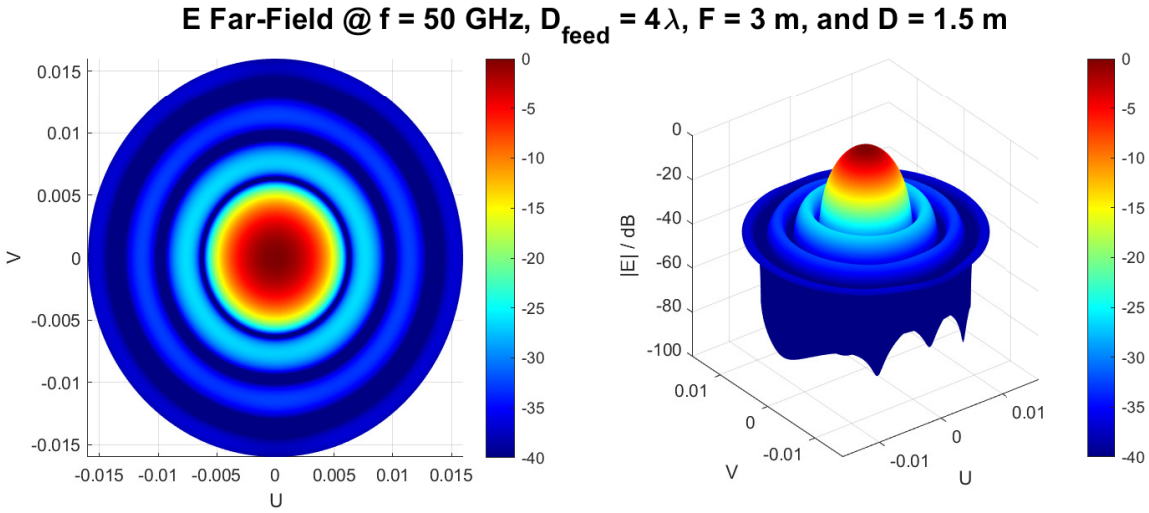

Fig. 5. Simulated aperture electric far-field $\vec{E}^{FF}$ pattern for the main and first three side lobes in decibels dB and normalized to the maximum value, for a frequency $f = 50\ GHz$, feed diameter $D_{feed} = 4\lambda$, aperture diameter $D = 1.5\ m$, and focal length $F = 3\ m$

diameter is greater than the feed's main lobe) resulting in larger beamwidth than calculated. Furthermore, as a consequence of the small beamwidth, the magnitude of $\vec{E}^{FF}$ is expected to be negligible as $\rho \to D/2$.

The simulated $\vec{E}^{FF}$ pattern (in dB at $f = 50\ GHz$, $D_{feed} = 4\lambda$, and $D = 1.5\ m$) is plotted for the main and first three side lobes in Fig.5; the plot is normalized to the maximum value. The simulated pattern coincides with the analytical expectations, the beamwidth is small, and consequently $\theta \to 0$ results in a properly defined airy pattern. However, as θ increases, the side lobes vary as a function of ϕ (as previously discussed). Yet, the $\vec{E}^{FF}$ magnitude decreases fast as ρ increases, resulting in negligible side lobes for the θ at which the lobes start the show the function of ϕ behaviour. Furthermore, the simulated $\vec{E}^{FF}$ magnitude compared to the magnitude of uniform equivalent aperture current (in dB at $f = 50\ GHz$, $D_{feed} = 4\lambda$, and $D = 1.5\ m$) at $\phi = 0°, 180°$ (XZ-plane) and $\phi = 90°, 270°$ (YZ-plane) is plotted in Fig.6; the plot is normalized to the maximum value. The simulation coincides with the analytical expectations, the actual beamwidth is slightly larger than that of the uniform aperture current, and the fields' magnitudes are equal in the XZ and YZ-planes. However, the side lobes of the uniform aperture field are larger (when compared to the main lobe) than the side lobes of the non-uniform aperture. Finally, the simulated uniform aperture far-field pattern (in dB at $f = 50\ GHz$ and $D = 1.5\ m$) is plotted for the main anf first three side lobes in Fig.7; the plot is normalized to the maximum value. The magnitude of the side lobes is larger compared to the main lobe than for the non-uniform aperture; in addition, due to the small θ, the side lobes are not a function of ϕ.

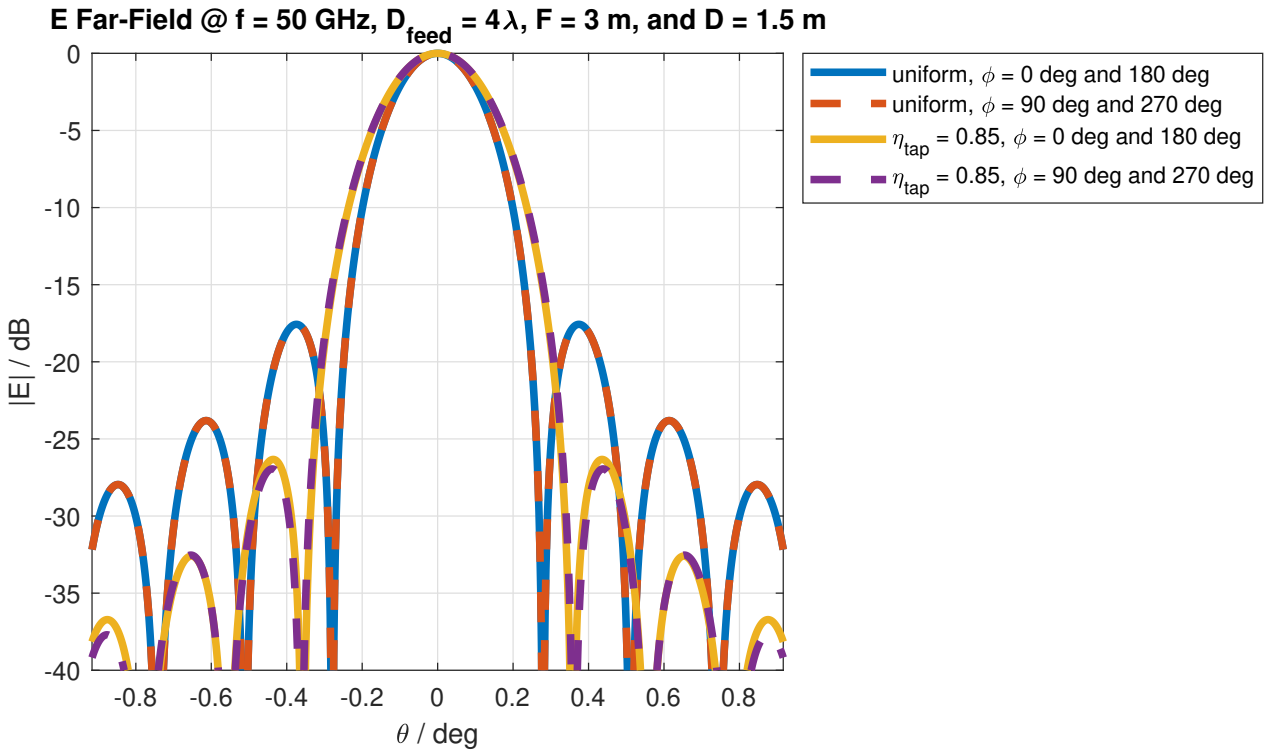

Fig. 6. Simulated aperture electric far-field $\vec{E}^{FF}$ compared to uniform aperture electric far-field in decibels dB and normalized to the maximum value, for a frequency $f = 50\ GHz$, feed diameter $D_{feed} = 4\lambda$, aperture diameter $D = 1.5\ m$, and focal length $F = 3\ m$; plotted at $\phi = 0°, 180°$ (XZ-plane) and $\phi = 90°, 270°$ (YZ-plane)

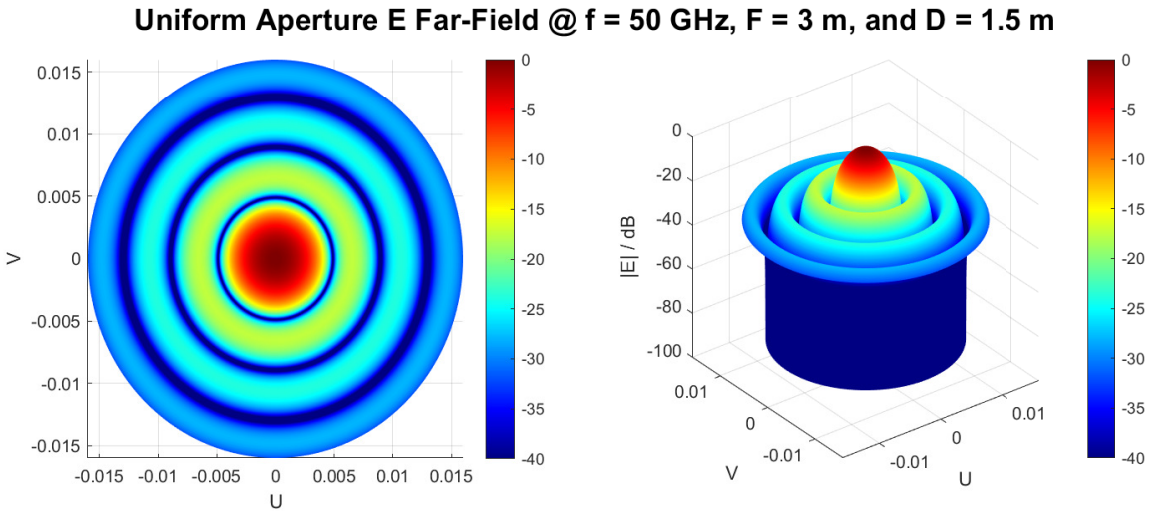

Fig. 7. Simulated uniform aperture electric far-field pattern for the main and first three side lobes in decibels dB and normalized to the maximum value, for a frequency $f = 50\ GHz$, aperture diameter $D = 1.5\ m$, and focal length $F = 3\ m$

IV. Taper, Spillover, and Aperture Efficiency

For the taper efficiency, it can be shown

$$\eta_{tap} = \frac{A_{eff}}{A} = \frac{1}{A}\frac{|\iint_S \vec{E}_a(\rho',\phi')dS|^2}{\iint_S |\vec{E}_a(\rho',\phi')|^2 dS}, \tag{14}$$

where A_{eff} is the antenna's effective are, and A is the antenna's physical area. As η_{tap} increases, A_{eff} approaches the physical area A. Intuitively, largest amount of power is radiated when the aperture current is uniformly distributed over the physical area. Moreover, the effective area is defined as the area that captures the receiving power when a plane wave is incident from broadside (as defined for a problem in reception). However, although the considered problem is in transmission, the aperture current densities result from the *incident* $\vec{E}_a$ on the equivalent aperture. Therefore the uniformity of the equivalent aperture currents (and by extension η_{tap}) are measured by the ratio of the effective and physical areas. As discussed, for small apertures, the reflected field at the reflector interface consists only of the $\vec{E}^{FF}_{feed}$ main lobe, resulting in an uniform aperture current distributions. Consequently, it is expected that at low diameters the taper efficiency approaches ones, while when increasing diameter, it decreases.

For the spillover efficiency, it can be shown

$$\eta_{so} = \frac{\int_0^{2\pi}\int_0^{\theta_0} U_{feed}(\theta',\phi')\sin\theta' d\theta' d\phi'}{\int_0^{2\pi}\int_0^{\pi/2} U_{feed}(\theta',\phi')\sin\theta' d\theta' d\phi'}, \tag{15}$$

where U_{feed} is the radiation intensity of the feed and θ_0 is the maximum angle at which the feed's field is reflected. Intuitively, η_{so} is a figure of merit, which quantifies the amount of reflected radiated feed power (the amount of used by the equivalent aperture). Therefore, it is expected that as the aperture diameter becomes larger more of feed's radiated power is reflected.

The aperture efficiency relates η_{tap} and η_{so} to the overall efficiency of the antenna

$$\eta_{ap} = \eta_{tap}\eta_{so}. \tag{16}$$

Consequently, it is expected that the largest aperture efficiency is achieved at the point of intersection between the taper and spillover efficiency. Moreover, as the aperture diameter increases the spillover efficiency approaches one, therefore it is expected that the aperture efficiency approaches the taper. For small diameters (resulting in uniform aperture currents), the taper efficiency is one and the aperture efficiency approaches the spillover.

The simulated η_{tap}, η_{so}, and η_{ap} (at $f = 50\ GHz$ and $D_{feed} = 4\lambda$) as a function of the aperture diameter are shown in Fig.8. The simulated efficiencies coincide with the analytical expectations, the taper efficiency decreases as the diameter increases (the equivalent aperture currents become less uniform), the opposite happens for the spillover efficiency which increases as the diameter increases (more of the feed's radiated power is reflected), and the aperture efficiency is highest close to the point of intersection between the taper and spillover efficiency. Finally, as the diameter increases the aperture efficiency approaches the taper efficiency, and as it decreases it approaches the spillover efficiency.

V. Maximum Directivity, Directivity, and Gain

For the maximum directivity, it can be shown that

$$\mathbb{D}_{max} = \frac{4\pi}{\lambda^2}A = \frac{4\pi}{\lambda^2}\frac{\pi D^2}{4}. \tag{17}$$

The maximum directivity is achieved when the aperture current densities are uniform (the effective area is equal to the physical area). Therefore it is proportionally related to the effective area (and by extension to the physical area). As the area increases, the assumption of the aperture currents uniformity does not change in the maximum directivity calculations, consequently, it is expected that the maximum directivity increases with the square of D.

As a consequence of the relation between maximum directivity and the uniformity of the aperture current densities, the actual directivity is related to the maximum directivity by η_{tap}

$$\mathbb{D} = \mathbb{D}_{max}\eta_{tap}. \tag{18}$$

Due to the decreasing η_{tap} with increasing diameter, it is expected that the actual directivity decreases as the aperture diameter increases.

Finally, the overall antenna gain is related to η_{ap} and $\mathbb{D}_{max}$

$$\mathbb{G} = \mathbb{D}_{max}\eta_{ap}. \tag{19}$$

Therefore, it is expected that the gain decreases as the aperture diameter increases. Furthermore, as the diameter increases, $\eta_{so} \to 1$ and consequently $\eta_{ap} \to \eta_{tap}$, which causes $\mathbb{D} \to \mathbb{G}$. On the other hand, as the diameter decreases, $\eta_{tap} \to 1$ and $\eta_{ap} \to \eta_{so}$ resulting in $\mathbb{D} \to \mathbb{D}_{max}$.

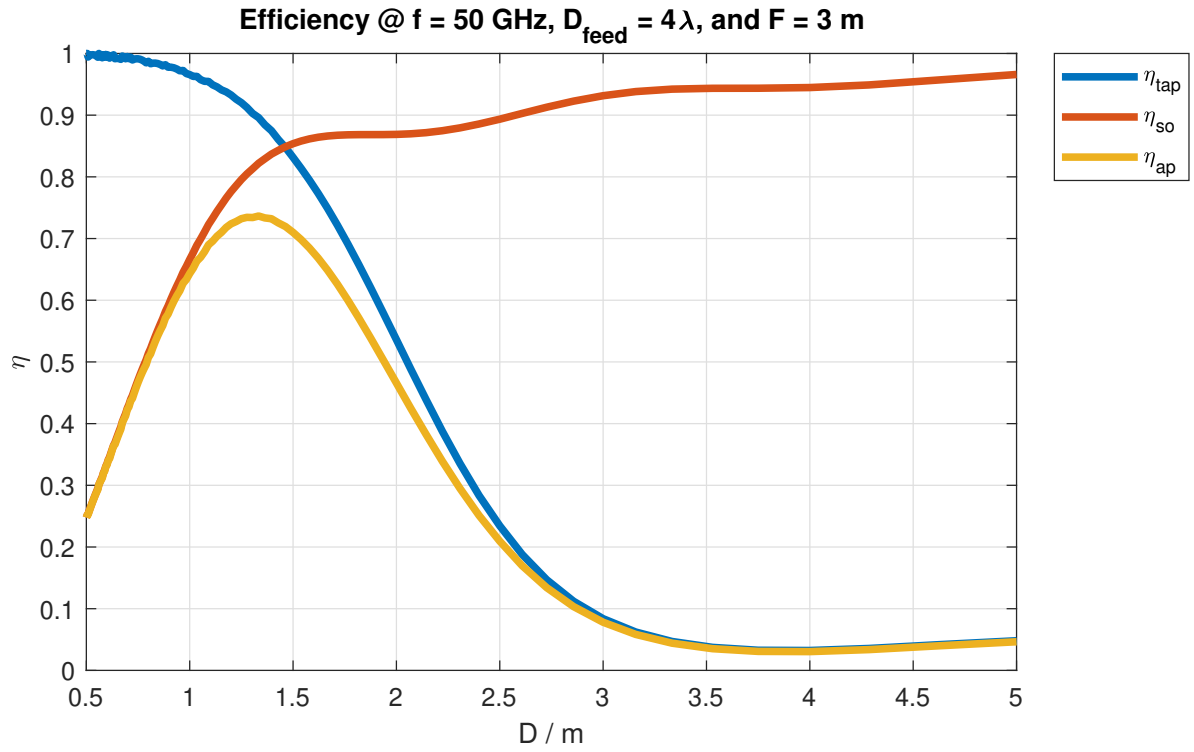

Fig. 8. Simulated taper η_{tap}, spillover η_{so}, and aperture η_{ap} efficiencies as a function of the aperture diameter D for a frequency $f = 50\ GHz$, feed diameter $D_{feed} = 4\lambda$, and focal length $F = 3\ m$

The simulated $\mathbb{D}_{max}$, $\mathbb{D}$, and $\mathbb{G}$ (in dB at $f = 50\ GHz$ and $D_{feed} = 4\lambda$) as a function of the aperture diameter are shown in Fig.9. The simulated maximum and actual directivity, and gain coincide with the analytical expectations, the directivity increases with the square of the diameter. Furthermore, initially the directivity approaches the maximum directivity (when the taper efficiency is high), and when the taper efficiency decreases and spillover efficiency increases, the directivity approaches the gain.

APPENDIX

The scripts used to simulate the parabolic reflector antenna are uploaded to the Git repository Assignment II Repository. And the library developed and used in the scripts is uploaded to quasi-optics-library. To run the simulations either place the script and library repositories in the same parent folder or change the library path in the simulation scripts.

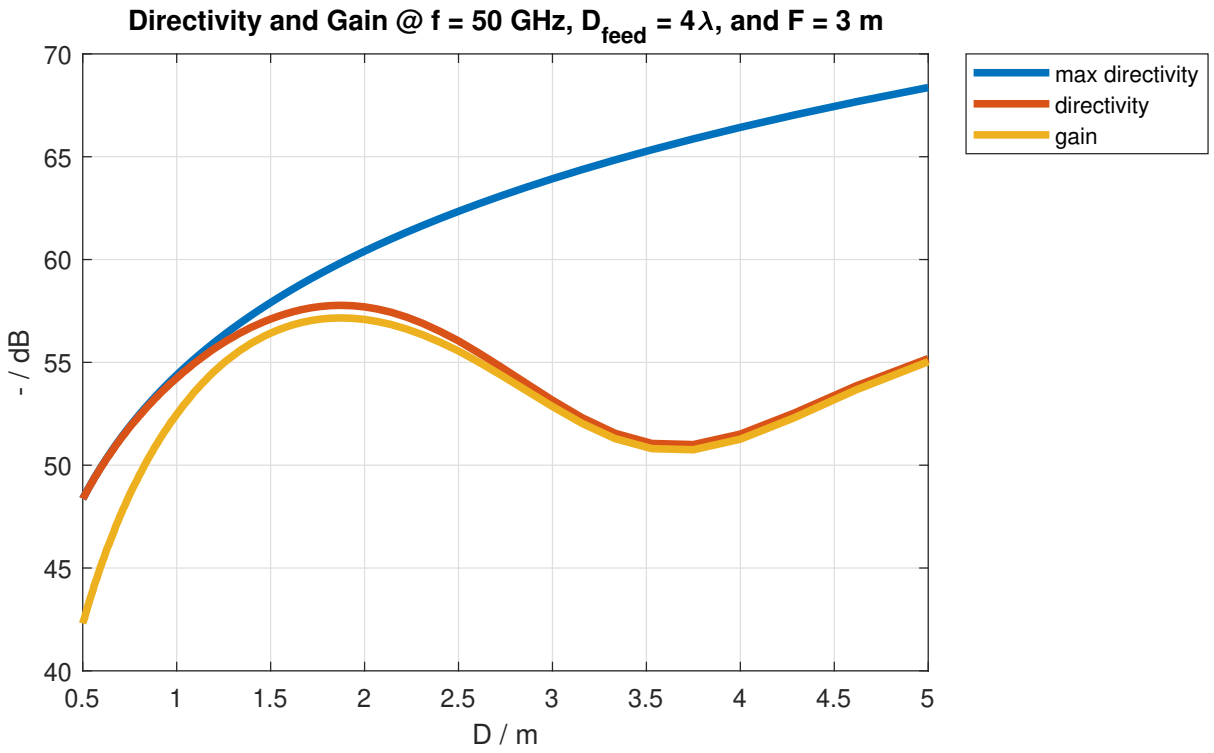

Fig. 9. Simulated maximum directivity $\mathbb{D}_{max}$, directivity $\mathbb{D}$, and gain $\mathbb{G}$ as a function of the aperture diameter D for a frequency $f = 50\ GHz$, feed diameter $D_{feed} = 4\lambda$, and focal length $F = 3\ m$